IOPscience iopscience.iop.org

Home Search Collections Journals About Contact us My IOPscience

Magnetic and magnetoelastic properties of epitaxial $SmFe_2$ thin film

This article has been downloaded from IOPscience. Please scroll down to see the full text article.

2010 J. Phys.: Condens. Matter 22 046004

(http://iopscience.iop.org/0953-8984/22/4/046004)

View the table of contents for this issue, or go to the journal homepage for more

Download details:
IP Address: 129.252.86.83
The article was downloaded on 30/05/2010 at 06:39

Please note that terms and conditions apply.

J. Phys.: Condens. Matter **22** (2010) 046004 (8pp) doi:10.1088/0953-8984/22/4/046004

Magnetic and magnetoelastic properties of epitaxial $SmFe_2$ thin film

C de la Fuente[1], J I Arnaudas[1,2], M Ciria[1], A del Moral[1], C Dufour[3] and K Dumesnil[3]

[1] Departamento de Magnetismo de Sólidos and Departamento de Física de la Materia Condensada, Instituto de Ciencia de los Materiales de Aragón and Universidad de Zaragoza, 50071, Zaragoza, Spain
[2] Instituto de Nanociencia de Aragón, Universidad de Zaragoza, 50071, Zaragoza, Spain
[3] Laboratoire de Métallurgie Physique et de Science des Matériaux, Université Henry Poincaré, Nancy 1, BP 239, 54506, France

E-mail: cesar@unizar.es

Received 8 October 2009
Published 12 January 2010
Online at stacks.iop.org/JPhysCM/22/046004

Abstract

We report on magnetic and magnetoelastic measurements for a 5000 Å (110) $SmFe_2$ thin film, which was successfully analyzed by means of a point charge model for describing the effect of the epitaxial growth in this kind of system. Some of the main conclusions of the Mössbauer and magnetoelastic results and the new magnetization results up to 5 T allow us to get a full description of the crystal electric field, exchange, and magnetoelastic behavior in this compound. So, new single-ion parameters are obtained for the crystal field interaction of samarium ions, $A_4\langle r^4\rangle = +755$ K/ion and $A_6\langle r^6\rangle = -180$ K/ion, and new single-ion magnetoelastic coupling $B^{\gamma,2} \simeq -200$ MPa and $B^{\varepsilon,2} \simeq 800$ MPa, which represent the tetragonal and the in-plane shear deformations, respectively. Moreover, the new thermal behavior of the samarium magnetic moment, the exchange coupling parameter, and the magnetocrystalline anisotropy of the iron sublattice are obtained too. From these, the softening of the spin reorientation transition with respect to the bulk case could be accounted for.

(Some figures in this article are in colour only in the electronic version)

1. Introduction

The cubic Laves-phases C15 RFe_2 (R = rare earth) are interesting from the technological point of view because most of them exhibit very large anisotropic magnetostriction at room temperature, especially, terfenol, $TbFe_2$ ($+1900$ μ defs) and samfenol, $SmFe_2$ (-2000 μ defs) [1, 2]. The strong spin–orbit coupling of the 4f electrons, about 400 K/ion [3, 4], is the origin of such large magnetostriction. However, RFe_2 also exhibits high magnetocrystalline anisotropy at low temperatures, which can raise coercive fields, but this is less interesting. In RFe_2, the dominant interaction is the exchange coupling between samarium and iron ions which leads to a ferromagnetic order. The competition between crystal electric field (CF) and the exchange is responsible for the spin reorientation transition observed in this compound. In past decades, the bulk $SmFe_2$ was found to have a spin reorientation transition at 150 K between the ⟨110⟩ easy-axis direction at low temperatures and ⟨111⟩ for higher ones [5, 6].

During the past few years, the wide development of the vacuum deposition techniques has allowed the growth of epitaxial RFe_2 thin films [7]. The study of the different factors associated with the epitaxial growing and their influence on the magnetic properties is still an open subject [8–20]. Certainly, this kind of study can lead to us finding the right way to control the magnetostriction of RFe_2 thin films for technological uses. Recently, (110) $SmFe_2$ thin films were thoroughly studied from the experimental structural and magnetic points of view [12, 13] and, later, from the magnetoelastic viewpoint [19].

In this paper, we present an extended study within the mean field approximation based on the use of point charges to describe the effect of epitaxy on the magnetic and magnetoelastic (MEL) behaviors. So, in the first section,

 © 2010 IOP Publishing Ltd Printed in the UK

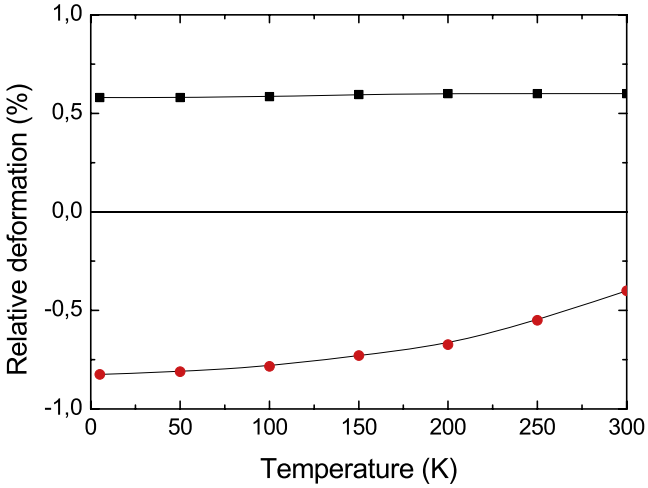

Figure 1. Epitaxial strain measured with the x-ray technique by means of the relative variation of the cubic lattice parameter $\Delta a/a$ along [004] and [220] directions. The solid square symbol represents the deformation in-plane along the [004] direction (it is the same behavior for deformations along $[2\bar{2}0]$), and the solid circle symbol shows the deformation perpendicular to the (110) plane, along the [220] direction. The lattice parameters, $a_{[220]} = 7.410$ Å, $a_{[2\bar{2}0]} \cong a_{[004]} = 7.440$ Å, at room temperature, are in good agreement with those for [11–13].

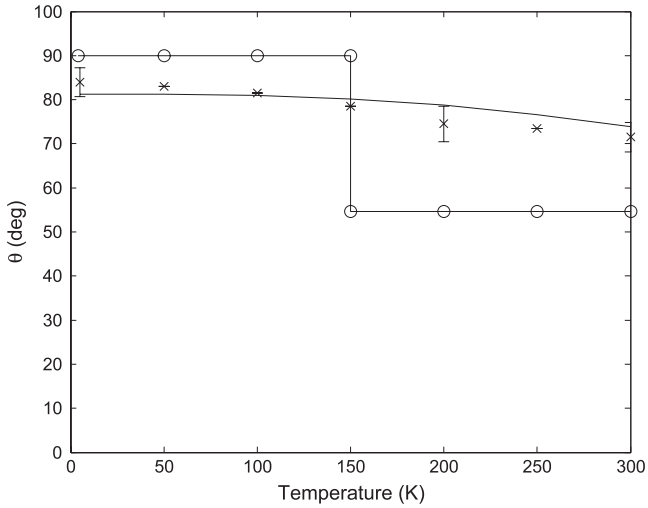

Figure 2. The temperature dependence of the θ values and $\varphi = 45°$ of the Sm^{3+} magnetic moment obtained from Mössbauer experiments for the bulk $SmFe_2$ (○, see [3, 4]) and (110) $SmFe_2$ (∗, see [11–13]). The continuous lines represent the calculated values with the model here presented.

we briefly detail the effect of epitaxy from a point charge model point of view. Then in section 2, we have studied the magnetism under the well-known mean field approximation, but adapted it for studying the epitaxial thin film samples. In section 3, we shall compare the experimental results from the orientation of spontaneous magnetization obtained from Mössbauer experiments and the results of calculations. In an additional section, we present novel experimental results from the field-forced magnetization along ⟨110⟩ and ⟨111⟩ directions. The results of calculations about the high-field behavior are also discussed in this section. Finally, we detail the model used to interpret our already published magnetoelastic stress experimental results [19] and present general conclusions.

2. Experimental details

The 5000 Å thick (110) $SmFe_2$ thin film, which we will consider for our calculations, was grown by molecular beam epitaxy, upon a thin (100 Å) YFe_2 seed on a (17 Å) NbFe-α layer covered with sapphire as substrate and capped by a thin yttrium film. X-ray diffraction showed good crystallinity in the epitaxial growth. For example, at room temperature, the (110) $SmFe_2$ thin film exhibits a lattice expansion within the (110) plane, $\epsilon_{[004]} = 0.6\%$, and a contraction along the growth direction, $\epsilon_{[220]} = -0.4\%$, because of the epitaxy. Figure 1 shows the summary of the experimental deformation within the (110) plane and along the [110] direction obtained from the analysis of the lattice parameters obtained from x-ray diffraction.

Mössbauer measurements were performed at room temperature in backscattering mode with a proportional gas-flow counter (He–5% CH_4). At low temperatures, reflection spectra were collected in a homemade cryostat equipped with a circular microchannel plate provided with a central hole. In order to get a reasonable counting rate, several hundred angstrom-thick samples were prepared with ^{57}Fe isotope enriched iron. Figure 2 shows the final analysis of the results for the samarium moments' orientation obtained from Mössbauer results for (110) $SmFe_2$ and the bulk results [11–13].

The magnetization curves were obtained by using a Quantum Design SQUID up to 5 T and between 5 K and room temperature. The external magnetic field will be applied within the (110) epitaxial plane. In the next lines, we will reference the ⟨111⟩ and ⟨110⟩ directions as the corresponding orientations within the (110) epitaxial plane. Figures 3(a) and 3(b) show the experimental magnetization measured along the ⟨111⟩ and ⟨110⟩ directions, respectively. As happened for (110) $TbFe_2/YFe_2$ epitaxial thin films [20], the (110) $SmFe_2$ thin film was also grown on a YFe_2 buffer, but in this case, the buffer is very small, just 100 Å thick. So, figures 3(a) and (b) show typically small features in the magnetization curves by the presence of the YFe_2 buffer. It is especially easy to see these features at low temperatures and near the coercive field.

The MEL stress was measured within the (110) plane of the epitaxial $SmFe_2$ thin film by using a capacitive technique from room temperature to 5 K, and in magnetic fields up to 12 T, applied along ⟨111⟩ in the in-plane direction. Details about the technique used can be found elsewhere, for example in [17]. Figure 4 shows the magnetoelastic stresses obtained by clamping the plate of the 'film and substrate' longitudinally, $\sigma_{\text{long.}}$, and transversely, $\sigma_{\text{trans.}}$, to the field direction applied along ⟨111⟩. The low temperature isotherms show a typical hysteresis behavior at low temperatures which is in good agreement with the magnetic hysteresis observed in

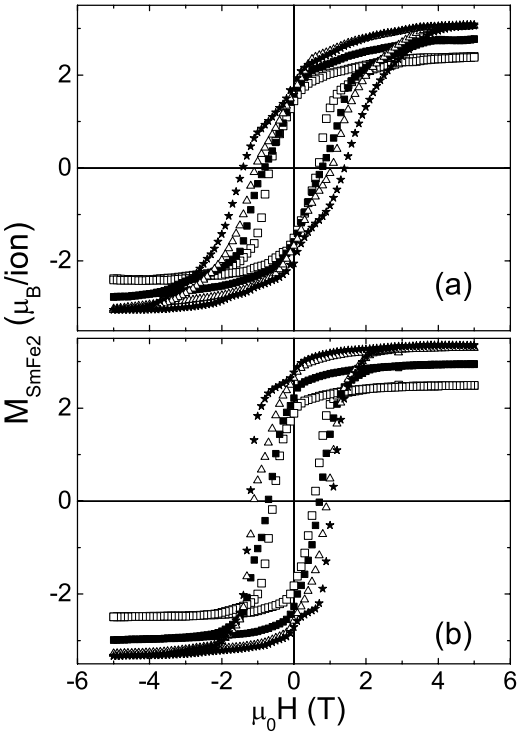

Figure 3. Experimental magnetization measured along the (a) ⟨111⟩ and (b) ⟨110⟩ directions, respectively, up to 5 T and for the temperatures 300 K— □, 200 K— ■, 100 K— ⋆ and 10 K— △.

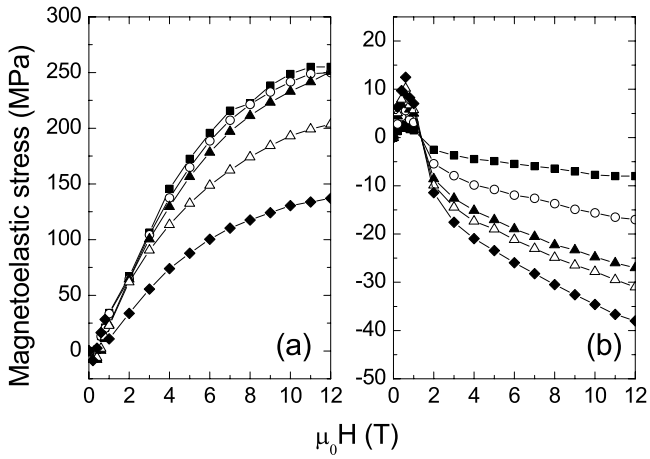

Figure 4. Magnetoelastic stress isotherms measured parallel (a) and perpendicular (b) to the field direction ⟨111⟩, up to 12 T. The lines are only visual guides (5 K— ■; 50 K— ○; 100 K— ▲; 200 K— △; 300 K— ♦).

magnetization curves with the field applied along ⟨111⟩ in the in-plane direction.

3. Effect of epitaxy on the local structure

The most important effect of the epitaxial growth is a slight reduction of the symmetry as compared to the original six-fold symmetry. Figure 5 shows qualitatively the old (solid circles) and new position (open circles) of the samarium

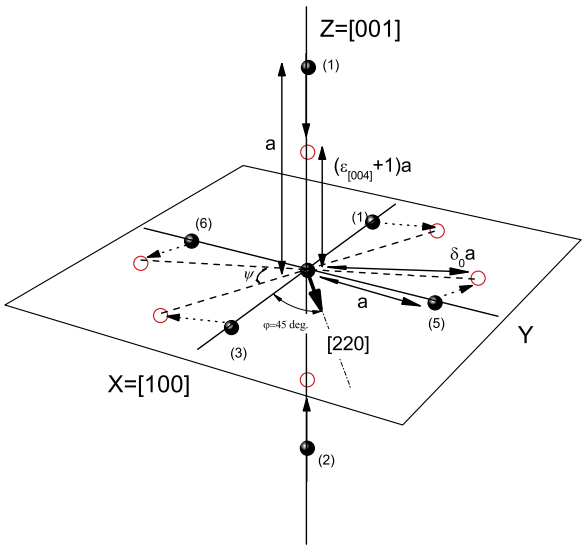

Figure 5. Qualitative illustration of the deformations induced by epitaxy on the Sm^{3+} ion environment for (110) $SmFe_2$ thin film. It shows the apparent lowering of the cubic six-fold symmetry by the epitaxial strain. The filled circle symbols represent the bulk positions of Sm^{3+} ions. The open circles represent the new positions of the samarium ions because of the deformation induced by epitaxy. Notice that [100] is the X-axis orientation and [001] the corresponding Z-axis.

ions without and with the existence of epitaxial deformation, respectively. Some of the geometric parameters are displayed in figure 5, and most of them can be easily related to the deformations, $\epsilon_{[004]}$ (deformation along the [001]-axis) and $\epsilon_{[220]}$ (deformation along the [220] direction which is perpendicular to the (110) thin-film plane), by using the equations listed in (1). Thus, the positions of samarium ions under epitaxial strain can be written in spherical coordinates as follows:

$$
\begin{aligned}
r_1 &= a(\epsilon_{[004]}+1), \qquad \theta_1 = 0,\\
r_2 &= a(\epsilon_{[004]}+1), \qquad \theta_2 = \pi,\\
r_3 &= \frac{a\delta_0}{2}, \qquad \theta_3 = \frac{\pi}{2},\\
\varphi_3 &= \arctan\left(-\frac{\epsilon_{[004]}-\epsilon_{[220]}}{\delta_0}, \frac{2+\epsilon_{[220]}+\epsilon_{[004]}}{\delta_0}\right),\\
r_6 &= \frac{a\delta_0}{2}, \qquad \theta_6 = \frac{\pi}{2},\\
\varphi_6 &= \arctan\left(-\frac{2+\epsilon_{[220]}+\epsilon_{[004]}}{\delta_0}, -\frac{\epsilon_{[004]}-\epsilon_{[220]}}{\delta_0}\right),\\
r_4 &= \frac{a\delta_0}{2}, \qquad \theta_4 = \frac{\pi}{2},\\
\varphi_4 &= \arctan\left(\frac{-\epsilon_{[220]}+\epsilon_{[004]}}{\delta_0}, \frac{2+\epsilon_{[220]}+\epsilon_{[004]}}{\delta_0}\right),\\
r_5 &= \frac{a\delta_0}{2}, \qquad \theta_5 = \frac{\pi}{2},\\
\varphi_5 &= \arctan\left(\frac{2+\epsilon_{[220]}+\epsilon_{[004]}}{\delta_0}, -\frac{\epsilon_{[004]}-\epsilon_{[220]}}{\delta_0}\right),
\end{aligned}
\tag{1}
$$

Table 1. List of non-null $\gamma_{n,m}$ terms used in (5) and (6). They depend in a non-linear way on the deformations ϵ_{zz} and ψ (see text for details). Notice that the bulk values are the corresponding ones existing in the literature for a cubic system like $SmFe_2$ (some of them are left in a non-compact form to illustrate the relevant factors that account for the CF for a pure six-fold symmetry [21]).

$\gamma_{n,m}$	(110) $SmFe_2$ thin film	$SmFe_2$ bulk
$\gamma_{2,0}$	$3.1706((1/(\epsilon_{zz}+1)^3)-1/\delta_0^3)$	0
$\gamma_{2,\pm2}$	$-0.3963\sqrt{6}(e^{\mp i2\psi}+e^{\pm i2(\pi-\psi)}+e^{\pm i2(\pi/2+\psi)}+e^{\pm i2(3\pi/2+\psi)})/\delta_0^3$	0
$\gamma_{4,0}$	$4.1357(0.5715/(\epsilon_{zz}+1)^5+0.4285/\delta_0^5)$	4.1357
$\gamma_{4,\pm2}$	$0.1777\sqrt{10}(e^{\mp i2\psi}+e^{\pm i2(\pi-\psi)}+e^{\pm i2(\pi/2+\psi)}+e^{\pm i2(3\pi/2+\psi)})/\delta_0^5$	0
$\gamma_{4,\pm4}$	$0.0738\sqrt{70}(e^{\mp i4\psi}+e^{\pm i4(\pi-\psi)}+e^{\pm i4(\pi/2+\psi)}+e^{\pm i4(3\pi/2+\psi)})/\delta_0^5$	$4\sqrt{70}(0.0738)$
$\gamma_{6,0}$	$0.7374(2.6665(1/(\epsilon_{zz}+1)^7)-1.6665/\delta_0^7)$	0.7374
$\gamma_{6,\pm2}$	$-0.0307\sqrt{105}(e^{\mp i2\psi}+e^{\pm i2(\pi-\psi)}+e^{\pm i2(\pi/2+\psi)}+e^{\pm i2(3\pi/2+\psi)})/\delta_0^7$	0
$\gamma_{6,\pm4}$	$-0.0921\sqrt{14}(e^{\mp i4\psi}+e^{\pm i4(\pi-\psi)}+e^{\pm i4(\pi/2+\psi)}+e^{\pm i4(3\pi/2+\psi)})/\delta_0^7$	$-4\sqrt{14}(0.0921)$
$\gamma_{6,\pm6}$	$-0.0307\sqrt{231}(e^{\mp i6\psi}+e^{\pm i6(\pi-\psi)}+e^{\pm i6(\pi/2+\psi)}+e^{\pm i6(3\pi/2+\psi)})/\delta_0^7$	0

where $\varphi_i \equiv \arctan(y,x)$, $-\pi \leqslant \varphi_i \leqslant \pi$, and the real arguments of the arctan-function computes a certain complex number $x+y\mathrm{i}$, which depends on $\epsilon_{[220]}$ and $\epsilon_{[004]}$; and

$$\delta_0 = \sqrt{(-\epsilon_{[220]}+\epsilon_{[004]})^2+(2+\epsilon_{[220]}+\epsilon_{[004]})^2}. \quad (2)$$

Notice that the angle, ψ, in figure 5, accounting for the xy in-plane shear deformation, can be calculated as $\varphi_3-\varphi_6 \equiv \varphi_4-\varphi_5=\psi$.

So, under small deformations, we can approximate $\psi \cong \pi/2+\epsilon_{xy}+\cdots$ and $\delta_0 \cong 1+\epsilon_{xx}+\cdots$. Then, we can relate ϵ_{xx} and ϵ_{xy} with the experimental deformations $\epsilon_{[220]}$ and $\epsilon_{[004]}$, as follows, $\epsilon_{xy} = (\epsilon_{[220]}-\epsilon_{[004]})/2$, $\epsilon_{xx} = (\epsilon_{[220]}+\epsilon_{[004]})/2$, $\epsilon_{xx} \cong \epsilon_{yy}$ and $\epsilon_{zz} = \epsilon_{[004]}$ (see figure 1). From those experimental deformations we can calculate the irreducible deformations associated with the tetragonal anisotropic deformation, $\epsilon_1^\gamma = (2\epsilon_{zz}-\epsilon_{xx}-\epsilon_{yy})/3 = (-\epsilon_{[004]}+\epsilon_{[220]})/3$, and with the xy in-plane shear deformation, $\epsilon_3^\epsilon = \epsilon_{xy}$.

The next model was thoroughly used in the early studies of RFe_2 bulk materials [3, 4]. Let us mention that it is here adapted for working with (110) RFe_2 thin films, applied to (110) $SmFe_2$ thin film. Then, the total free energy can be written as

$$F_{SmFe_2} = -k_B T \ln Z_{Sm}(\theta,\varphi) + \frac{K_1^{(Fe)}}{32}(7-4\cos 2\theta-3\cos 4\theta). \quad (3)$$

The first term is the samarium contribution to the total free energy, and the second one is the iron contribution to the magnetocrystalline anisotropy, where, $K_1^{(Fe)}$ represents the intensity of this anisotropy; the (θ,φ) values account for the angular part of the spherical coordinates of samarium or iron magnetic moments, ferromagnetically coupled by exchange. Thus, the partition function of samarium, $Z_{Sm}(\theta,\varphi)$, can be written as

$$Z_{Sm}(\theta,\varphi) = \mathrm{Tr}\left[\exp\left(-\frac{H_{CF}+H_{MEL}+\lambda_{so}\vec{L}\cdot\vec{S}-\mu_B\overrightarrow{B}_{eff.}\cdot\overrightarrow{M}_{Sm}}{k_B T}\right)\right], \quad (4)$$

where λ_{so} is the spin–orbit coupling parameter, $\overrightarrow{B}_{eff}$ is an effective magnetic field which includes:

(1) the externally applied magnetic field, $\overrightarrow{B}_{ap.} = \mu_0 \overrightarrow{H}_{ap.}$;
(2) the demagnetizing field, $\overrightarrow{B}_d$ which depends on the total magnetization of $SmFe_2$, $\overrightarrow{M}_{SmFe_2}$;
(3) the dominant exchange mean field, which is proportional to the iron sublattice magnetization, $\overrightarrow{B}_{ex.} = \lambda_{ex}\overrightarrow{M}_{Fe}$.

The $\vec{L}$ and $\vec{S}$ present in (4) are rank one tensor operators and $\overrightarrow{M}_{Sm}$ is the magnetization of samarium ions. The CF contribution can be easily calculated following the classical method illustrated by Hutchings in [21],

$$H_{CF} = A_4\langle r^4\rangle\gamma_{4,0}[Y_4^0+\sqrt{5/14}(Y_4^4+Y_4^{-4})] + A_6\langle r^6\rangle\gamma_{6,0}[Y_6^0-\sqrt{7/2}(Y_6^4+Y_6^{-4})]. \quad (5)$$

The single-ion MEL energy in (4), written only up to the highest second-order contribution, reads as

$$H_{MEL} = A^{\gamma,2}\langle r^2\rangle\gamma_{2,0}Y_2^0 + A^{\epsilon,2}\langle r^2\rangle\gamma_{2,|\pm2|}\mathrm{i}(Y_2^{-2}-Y_2^2)+\cdots, \quad (6)$$

where $A^{\gamma,2}\langle r^2\rangle$ and $A^{\epsilon,2}\langle r^2\rangle$ are the second-order MEL parameters. Table 1 shows the values obtained for $\gamma_{n,m}$ under epitaxial strain and without it. Notice that the $\gamma_{2,0}$ and $\gamma_{2,|\pm2|}$ coefficients have a main lower order contribution which depends linearly on the strains ϵ_1^γ and ϵ_3^ε. By taking into account only this low order term, we recover from (6) the well-known linear MEL energy which can be found elsewhere in the literature.

To end this section, let us mention that the total energy (3) is self-consistently solved for a correct accounting of demagnetizing field in the studied thin film by using as seed the results of a calculation without considering the demagnetizing field.

4. Analysis and discussion of the experimental results

4.1. Mössbauer results

The zero-field Mössbauer results were used to determine the CF parameters, $A_4\langle r^4\rangle$ and $A_6\langle r^6\rangle$. Figure 6 represents the θ-values of the samarium magnetic moment at 5 K with respect to the crystallographic direction [001] for different CF values; thus, the blue region is the orientation along the [001]-axis. Figure 7 is similar to figure 6 but for φ values around the z-axis, within the xy plane; the blue region representing the

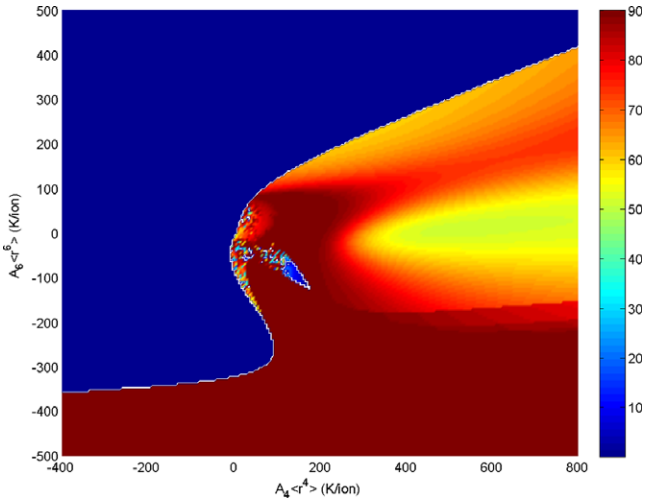

Figure 6. Surface plot showing the θ-values of the Sm^{3+} magnetic moment at 5 K with respect to the [001] direction versus the CF parameters $A_4\langle r^4\rangle$ and $A_6\langle r^6\rangle$ for a set of fixed values of model parameters (see footnote 4). The color bar on the right represents the degrees of the angular scale of θ-values.

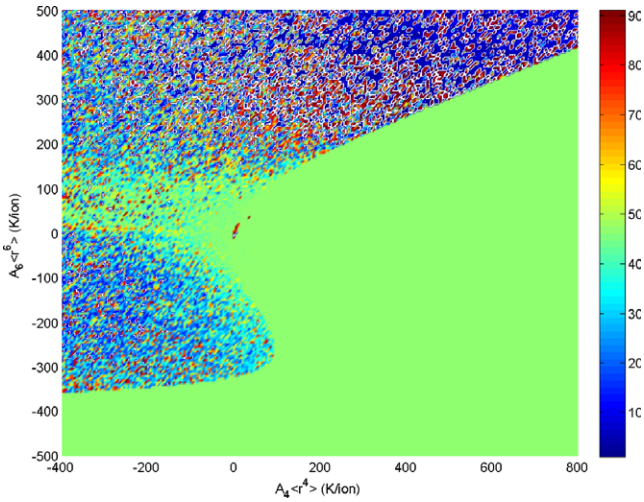

Figure 7. Surface plot showing the φ values' dependence of the Sm^{3+} magnetic moment at 5 K with respect to the [100] direction versus the CF parameters, $A_4\langle r^4\rangle$ and $A_6\langle r^6\rangle$, for a set of fixed values of model parameters (see footnote 4). The color bar on the right represents the degrees of the angular scale of φ values. Notice that the (110) plane of the epitaxial thin film is represented by the green color given by $\varphi = 45°$.

Table 2. Calculated magnetic moment values (μ_B/ion) at different temperatures in the absence of any external magnetic field for $SmFe_2$ bulk and thin film.

	$SmFe_2$ bulk[a]			(110) $SmFe_2$ thin − film[b]	
$T(K)$	M_{SmFe_2}	M_{Sm}	M_{Fe}	M_{SmFe_2}	M_{Sm}
8	2.87	0.53	2.34	3.28	0.94
50	2.86	0.53	2.33	3.27	0.94
100	2.91	0.62	2.29	3.22	0.93
155	2.97	0.75	2.22	3.06	0.84
200	2.98	0.84	2.14	2.86	0.72
250	2.93	0.90	2.03	2.62	0.59
300	2.81	0.92	1.89	2.36	0.47

[a] See [3, 4]. [b] See footnote 4.

orientation along [100], within the (001) plane. The couple of CF parameters $A_4\langle r^4\rangle = +755$ K/ion and $A_6\langle r^6\rangle = -180$ K/ion were the optimal ones giving the best fit for the thermal dependence of the angle θ (see figure 2). Notice that, in the fitting process, the model parameters are those values[4] also used in the analyses of magnetization and magnetoelastic stress experimental results (see next sections 4.2 and 4.3). Figure 2 also displays the fit obtained for the bulk $SmFe_2$ results, using the existing CF, exchange and anisotropy parameters [3, 4]; this represents a check of the zero-strain limit of our model. Table 2 summarizes all the spontaneous magnetization values obtained from these calculations.

The values of the magnetocrystalline anisotropy constant of the iron sublattice, $K_1^{(Fe)}$, and the exchange constant, λ_{ex}, obtained for the film are slightly smaller, $\simeq$12%, than the bulk ones. This could indicate the existence of higher order MEL contributions, or even, non-linear MEL terms in the macroscopic free energy of the iron sublattice, not accounted for in (3) [22, 23]. Unfortunately, there is no way to decide which is the case, so, it has to be left as an open question to be answered by studying, for example, an itinerant magnet such as a (110) YFe_2 thin film.

[4] $A_4\langle r^4\rangle = +755$ K/ion, $A_6\langle r^6\rangle = -180$ K/ion, $A^{\gamma,2}\langle r^2\rangle = -160$ K/ion, $A^{\varepsilon,2}\langle r^2\rangle = -550$ K/ion, $K_1^{(Fe)} = -1.7$ K/ion, $\lambda_{ex} = 53.3$ K/ion; the modulus of M_{Fe} is the same as for the bulk case.

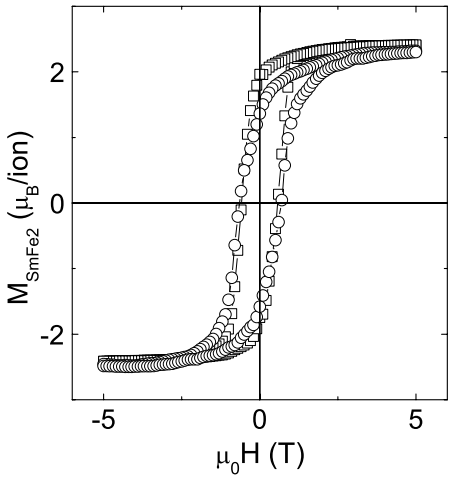

Figure 8. Experimental magnetization (in μ_B/ion) of $SmFe_2$ at 300 K for a magnetic field applied along ⟨111⟩ (○,) and ⟨110⟩ (□) directions. Notice that the buffer contribution of the YFe_2 seed is now eliminated (see details in the text).

4.2. High-field magnetization

Figure 8 shows the $SmFe_2$ magnetization at room temperature, but in this case without the contribution of YFe_2 (see [20] for details). After subtraction of the YFe_2 contribution, figure 9(a) shows the magnetic moment of $SmFe_2$ along ⟨111⟩ and ⟨110⟩ directions at room temperature and for the maximum

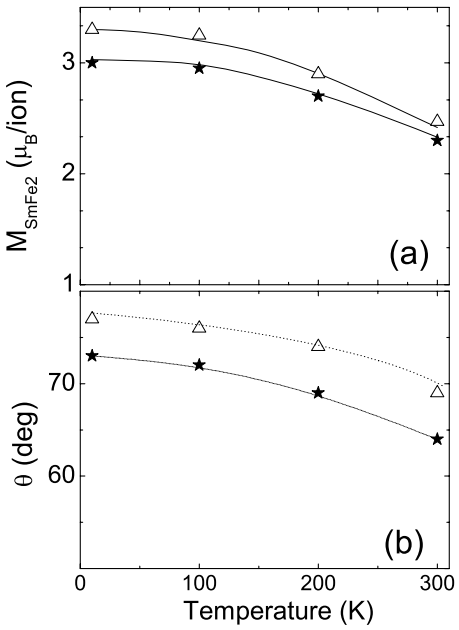

Figure 9. (a) Thermal evolution of the samarium magnetic moment orientation, θ within the (110) plane at the maximum applied field, 5 T △—⟨110⟩ and ⋆—⟨111⟩ applied field directions. The continuous lines represent the calculated values with the model here presented. (b) The thermal dependence of the θ values obtained from a magnetic field extrapolation up to 12 T, △—⟨110⟩ and ⋆—⟨111⟩ field directions. The dashed lines are only visual guides.

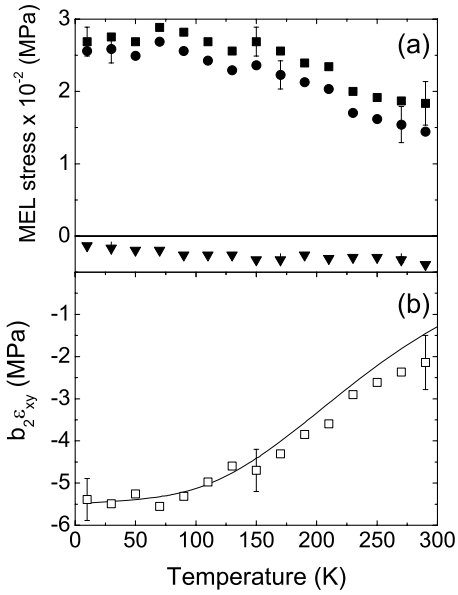

Figure 10. (a) The MEL stress values measured along $\sigma_{||}$ (▼) and transversely, $\sigma_{\perp}$, (●) to the field direction, ⟨111⟩ at the maximum field applied externally, 12 T, in a (110) $SmFe_2$ thin film; the thermal dependence of $\sigma_{||} - \sigma_{\perp}$ (■) (see (12)) is also represented. (b) The experimental $b_2\epsilon_{xy}$ (□) and the calculated contribution obtained using (13).

field, 5 T. These high-field values were also calculated by including the corresponding Zeeman contribution along ⟨110⟩ and ⟨111⟩ directions, and keeping constant the rest of the model parameters obtained in section 4.3. Thus, the continuous lines give the best fits for both directions. The quality of the fits gives us confidence in the model used to explain some magnetic properties of our epitaxial $SmFe_2$ thin film.

On the other hand, we shall see later how this model also works in the analysis of MEL contributions. For this purpose, let us advance some additional information that we shall use later. Figure 9(b) displays the θ-values of the samarium magnetic moment obtained from the magnetization measured at high fields, applied along ⟨111⟩ and ⟨110⟩ directions, $\theta(\overrightarrow{B}_{\text{ap.}})$. Two different kinds of θ values are displayed in this figure: the first type comes directly from the high-field values obtained in figure 9(a), where the magnetization along ⟨110⟩, at 5 T, could be considered as almost saturated, as the calculations confirm; the second one represents the θ values obtained from the linear extrapolation from 4 to 5 T up to 12 T, where the MEL experimental results will be analyzed (as we will see in section 4.3).

4.3. Magnetoelastic stress

Figure 10(a) shows the values of $\sigma_{\text{long}} - \sigma_{\text{trans}}$, at 12 T, obtained from figures 4(a) and (b). Notice that the obtainment of the relevant MEL parameter corresponding to the shear stress in bulk $SmFe_2$ is performed by analyzing $\sigma_{\text{long}} - \sigma_{\text{trans}}$ [1, 2]. In the case of a thin film grown on a substrate, to characterize the MEL behavior, it is necessary to correlate the stress and the curvature of the 'film + substrate' induced by the external field, $\overrightarrow{B}_{\text{ap}}$; this is done by using the theory of pure bending plates [24], as was done previously for similar systems [17, 18, 20]. When the thin film is clamped along different directions, we should calculate its total MEL and elastic energy, E_{tot}. In this procedure we consider that the MEL energy density of $SmFe_2$ is quadratic in the magnetization components and linear in the strains, so

$$\begin{aligned} e_{\text{MEL}}^{\text{SmFe}_2} \equiv e_{\text{MEL}}^{\text{SmFe}_2}(\alpha_x, \alpha_y, \alpha_z) &= b_0(\epsilon_{xx} + \epsilon_{yy} + \epsilon_{zz}) \\ &+ b_1(\alpha_x^2\epsilon_{xx} + \alpha_y^2\epsilon_{yy} + \alpha_z^2\epsilon_{zz}) \\ &+ b_2(\alpha_x\alpha_y\epsilon_{xy} + \alpha_x\alpha_z\epsilon_{xz} + \alpha_y\alpha_z\epsilon_{yz}) \\ &+ \tfrac{1}{2}c_{11}(\epsilon_{xx}^2 + \epsilon_{yy}^2 + \epsilon_{zz}^2) \\ &+ c_{12}(\epsilon_{xx}\epsilon_{zz} + \epsilon_{yy}\epsilon_{zz} + \epsilon_{xx}\epsilon_{yy}) \\ &+ \tfrac{1}{2}c_{44}(\epsilon_{xy}^2 + \epsilon_{xz}^2 + \epsilon_{yz}^2). \end{aligned} \tag{7}$$

Equation (7) is written in the usual coordinate axes $OXYZ$. Thus, α_i $(i = x, y, z)$ are the director cosines of the magnetization M_{SmFe_2}; ϵ_{ij} $(i, j = x, y, z)$ are the Cartesian strain components that will be dependent on the magnetization value and orientation at equilibrium; c_{11}, c_{12} and c_{44} are the Cartesian stiffness constants of $SmFe_2$ [25], b_2 is the MEL stress giving rise to the cubic cell deformation, ϵ_{xy}, i.e. the deviation of the angle between neighboring edges of the distorted cube from $\pi/2$ or the rhombohedral deformation; b_1 is the MEL stress producing the tetragonal deformation, $\Delta a/a$; and b_0 is the MEL stress related to a combination of volume MEL and tetragonal strains (see figure 5).

After the minimization of the total energy from the (110) $SmFe_2$ thin film and the substrate, we get the radius of

curvature of the plate, R, at equilibrium (or the corresponding stresses, commented on above) as a function of the MEL stress parameters

$$\frac{\partial E_{\rm tot}(\overrightarrow{B}_{\rm ap.} \parallel \langle 111\rangle)}{\partial R_{y''}^{-1}} = \sigma_{\rm long.} + \frac{2(c_{11}-c_{12}+4c_{44})}{3(c_{11}+c_{12}+2c_{44})}b_0 + \frac{(c_{11}+2c_{12}+c_{44})\cos(2\theta)+c_{11}+3c_{44}}{3(c_{11}+c_{12}+2c_{44})}b_1 + \{(c_{11}+3c_{12})(1-\cos 2\theta)-2\sqrt{2}(c_{11}+c_{12}+2c_{44}) \times \sin 2\theta\}\{6(c_{11}+c_{12}+2c_{44})\}^{-1}b_2 = 0 \quad (8)$$

$$\frac{\partial E_{\rm tot}(\overrightarrow{B}_{\rm ap.} \parallel \langle 111\rangle)}{\partial R_{z''}^{-1}} = \sigma_{\rm trans.} + \frac{(c_{11}-c_{12}+10c_{44})}{3(c_{11}+c_{12}+2c_{44})}b_0 + \frac{(c_{11}+2c_{12}-2c_{44})\cos(2\theta)+c_{11}+6c_{44}}{6(c_{11}+c_{12}+2c_{44})}b_1 + \{(2c_{11}+3c_{12})(1-\cos 2\theta)+2\sqrt{2}(c_{11}+c_{12}+2c_{44}) \times \sin 2\theta\}\{6(c_{11}+c_{12}+2c_{44})\}^{-1}b_2 = 0 \quad (9)$$

where

$$\sigma_{\rm long.} = \frac{1}{6}\frac{h_{\rm sapphire}^2}{h_{\rm SmFe_2}}\left(\frac{C_{y''y''}^{\rm sapphire}}{R_{y''}} + \frac{C_{y''z''}^{\rm sapphire}}{R_{z''}}\right), \quad (10)$$

$$\sigma_{\rm trans.} = \frac{1}{6}\frac{h_{\rm sapphire}^2}{h_{\rm SmFe_2}}\left(\frac{C_{z''z''}^{\rm sapphire}}{R_{z''}} + \frac{C_{y''z''}^{\rm sapphire}}{R_{y''}}\right). \quad (11)$$

Let us notice that (8)–(11) are referred to a coordinate system $OX''Y''Z''$, that has been obtained from our original coordinate system $OXYZ$ ($OXYZ$ is the same as in figure 5) after a two-stage rotation procedure[5]. In this way, the cut edges of our film are parallel and perpendicular to $OY'' \parallel \langle 111\rangle$. In (10) and (11), $h_{\rm sapphire}$ and $h_{\rm SmFe_2}$ are the sapphire and $SmFe_2$ thin-film thickness, respectively; $C_{i''j''}^{\rm sapphire}$ the elastic constants of sapphire [26], $R_{z''}$ and $R_{y''}$ are the radii of curvature of the plate for clamping along the Y''- and Z''-axes, respectively (those radii are, in fact, the measured quantities through the capacitive technique mentioned above).

A combination of the relevant MEL stress parameters is then obtained from (8) and (9),

$$\sigma_{\rm long} - \sigma_{\rm trans} = \frac{1}{3}\left[\frac{c_{12}-c_{11}+2c_{44}}{c_{11}+c_{12}+2c_{44}}\right]b_0 - \frac{1}{6}\left[\frac{c_{11}}{c_{11}+c_{12}+2c_{44}} + \frac{c_{11}+2c_{12}+4c_{44}}{c_{11}+c_{12}+2c_{44}}\cos(2\theta)\right]b_1 - \frac{1}{6}\left[4\sqrt{2}\sin(2\theta) + \frac{c_{11}}{c_{11}+c_{12}+2c_{44}} \times (1-\cos(2\theta))\right]b_2, \quad (12)$$

where θ is the magnetic moment orientation of Sm^{+3}, at 12 T, within the (110) plane when the magnetic field is applied along $\langle 111\rangle$, and it can be obtained from magnetization measurements performed by applying the magnetic field along $\langle 111\rangle$ and $\langle 110\rangle$ directions (as was mentioned in the preceding section). Notice that the 12 T magnetization values needed have been obtained by a linear extrapolation of the high-field measurements (see figure 9(b)).

In addition, let us observe that there is no way to get b_2, b_1, and b_0 as independent parameters from our MEL measurements with the field just applied along $\langle 111\rangle$, as was done in previous works [20]. So, we shall assume that b_1 and b_0 terms are negligible. Let us analyze the reason for that. For this purpose, we should use the values of figure 9(b) to calculate the relative weight of each MEL contribution in (12). Thus, if we assume an average value for $\theta \simeq 71.6°$, at 12 T, within the whole measurement range of temperatures, then $\langle\cos 2\theta\rangle \approx -0.75$ and $\langle\sin 2\theta\rangle \approx 0.6$. So, (12) can be approximated by $\sigma_{\rm long} - \sigma_{\rm trans} \approx 0.048b_0 + 0.125b_1 - 0.68b_2$. A quick look at this equation indicates to us that the coefficient of the b_0-term has a very small value compared with those of b_1 and b_2 terms. Certainly, the contribution to $\sigma_{\rm long} - \sigma_{\rm trans}$ of the total b_0-term should depend on the real magnitude of the b_0 MEL parameter. Although there are not many works in the literature where the MEL parameter b_0 had been obtained from experiment, it has been done for similar systems, such as the (110) $TbFe_2/YFe_2$ thin films [20]. Assuming that in (110) $SmFe_2$ the coefficient b_0 has the same order of magnitude, we could approximate $\sigma_{\rm long} - \sigma_{\rm trans}$ by just $+0.125b_1 - 0.68b_2$.

In this way, the results of the model here presented directly give us $b_1 = 3B^{\gamma,2}/2$ and $b_2 = B^{\varepsilon,2}$ MEL parameters [1] (see footnote 6). Thus, accordingly with the values given in footnote 5, the values of the MEL parameters are $B^{\gamma,2} \simeq -200$ MPa and $B^{\varepsilon,2} \simeq 800$ MPa,[6] both having about the same order of magnitude and opposite signs. Considering these values, we can reasonably approximate $\sigma_{\rm long} - \sigma_{\rm trans} \simeq -0.68b_2$. So, the relationship between the b_2 MEL stress parameter and the measured MEL stresses from (12) reduces to

$$b_2 \simeq \frac{6(\sigma_{\rm long} - \sigma_{\rm trans})}{4\sqrt{2}\sin(2\theta) + \frac{c_{11}}{c_{11}+c_{12}+2c_{44}}(1-\cos(2\theta))}. \quad (13)$$

Figure 10(b) displays the experimental values of $b_2\epsilon_{xy}$, b_2 being obtained from (13) and ϵ_{xy} the irreducible deformation induced by epitaxy. This figure also displays the corresponding calculated values from the mean field model by using basically the following expression, valid for the linear regime of strains

$$A^{\epsilon,2}\langle r^2\rangle\gamma_{2,|\pm 2|}\,{\rm i}\langle Y_2^{-2} + Y_2^2\rangle_T = b_2\epsilon_{xy}. \quad (14)$$

Notice that the agreement between the MEL stress experimental results and theory is good, especially at low temperatures, without modifying any of the parameters previously obtained to explain magnetization data. This means that the difference between the non-linear effects of deformations induced by epitaxy in the total MEL energy (see (6)) and the linear effects is very small, especially at low temperatures. However, these differences become more important at high temperature where,

[5] The first rotation is of 45° around the first z-axis; the second one is a rotation of 54.73°. around the intermediate x'-axis of $OX'Y'Z'$.

[6] $b_1 = 3/2B^{\gamma,2}$, $B^{\gamma,2} = (4.7559)(A^{\gamma,2}\langle r^2\rangle)$, and $b_2 = B^{\varepsilon,2} = \sqrt{2}(-3.8529)(A^{\varepsilon,2}\langle r^2\rangle)$.

surprisingly, the epitaxial deformations are lower than the low temperature ones. That could be assigned to the influence of the non-linear MEL part of (6), clearly not accounted for in (7) to get b_2, or by a poor approximation done to get (14) where b_1 was neglected.

Finally, and in accordance with [1], we can estimate the magnetic rhombohedral external distortion along the ⟨111⟩ direction, $\lambda_{\langle 111\rangle} = -B^{\varepsilon,2}/(3c_{44})$, and the ⟨100⟩ cubic case, $\lambda_{\langle 100\rangle} = -B^{\gamma,2}/(c_{11} - c_{12})$, for the (110) $SmFe_2$ thin film. These estimations show us that $\lambda_{\langle 111\rangle} = -1.2\%$ and $\lambda_{\langle 100\rangle} = +0.9\%$, in the 0 K limit. These values are completely different from the bulk case because both are strongly enhanced, especially $\lambda_{\langle 100\rangle}$. Definitely, the cubic deformation $\lambda_{\langle 100\rangle}$ in (110) $SmFe_2$ thin film is enhanced with respect to the magnetic deformations for the bulk case, under a strong applied magnetic field. From the point of view of the atomic model proposed by Clark and Cullen [1, 2, 27], the potentially huge value of $\lambda_{\langle 100\rangle}$ arising from the asymmetry of the Sm^{3+} shell is not fully shorted out as in the bulk case. The reason for this is that the high tetrahedral symmetry at the Sm^{3+} is now broken, or lifted, by the relevant (110) in-plane epitaxial deformation along the z-axis in (110) $SmFe_2$ thin film (see figure 5). On the other hand, the internal distortions along the ⟨111⟩ direction certainly should still favor the lowering of the symmetry as in the bulk case. In the (110) $SmFe_2$ case, parts of the rhombohedral deformations are induced by the epitaxy, and other are introduced by the application of a magnetic field which is directed along the ⟨111⟩-axis. The shear strain epitaxial contribution at low temperatures is -0.7%, while the effective rhombohedral distortion we can obtain is $\lambda_{\langle 111\rangle} = -1.2\%$ at 12 T. These different values represent the real magnetostriction induced by the magnetic field at 12 T, -0.5%, which is relatively close to the bulk value ($\approx -0.4\%$ for just 2.5 T from [1, 2]). In this sense, the epitaxy effectively works by driving our system to an initial magnetostrictive state, where the rhombohedral deformations induced by the applied field strongly enhance the existing epitaxial ones.

5. Summary

The effect of epitaxial strain on the magnetic and MEL properties of (110) $SmFe_2$ thin film has been analyzed by using a quite simple mean field model. From this analysis we have deduced that the exchange coupling parameter and the magnetocrystalline anisotropy of the iron sublattice change, as compared with the bulk values, which could be ascribed to high order or non-linear MEL contributions to the total free energy. Moreover, new crystal field and magnetoelastic parameters have been obtained taking into account the tetragonal and the in-plane shear deformations induced by the epitaxy. The good agreement between our calculations and the experimental results supports the validity of the performed analysis.

Acknowledgments

The authors acknowledge Dr L Benito and the financial support given by the Spanish projects FIS2006-09113, MAT2009-10040, and DGA project PI049/08 and grant E-81.

References

[1] Clark A E 1982 *Handbook of the Physics and Chemistry of Rare Earth* vol 2, ed K A Gschneidner and L Eyring (Amsterdam: North-Holland) and references therein
[2] Clark A E 1980 *Ferromagnetic Materials* vol 1, ed E P Wohlfarth (Amsterdam: North-Holland) and references therein
[3] van Diepen A M, de Wijn H W and Buschow K H J 1973 *Phys. Rev.* B **8** 1125
[4] de Wijn H W, van Diepen A M and Buschow K H J 1973 *Phys. Rev.* B **7** 524
[5] Wallace W E and Scrabek A E 1964 *Rare Earth Research* vol 2 (New York: Gordon and Breach) p 431
[6] Buschow K H J and van Stapele R P 1971 *J. Physique* **32** (Suppl.) C1-672
[7] Oderno V, Dufour C, Dumesnil K, Mangin Ph and Marchal G 1996 *J. Growth* **162** 175
[8] Oderno V, Dufour C, Dumesnil K, Bauer Ph, Mangin Ph, Marchal G, Hennet L and Patrat G 1996 *Europhys. Lett.* **36** 713
[9] Oderno V, Dufour C, Dumesnil K, Bauer Ph, Mangin Ph and Marchal G 1996 *Phys. Rev.* B **54** R17375
[10] Oderno V 1996 *PhD Thesis* Institut National Polytechnique de Lorraine, France
[11] Mougin A, Dufour C, Dumesnil K, Maloufi N and Mangin Ph 1999 *Phys. Rev.* B **59** 5950
[12] Mougin A, Dufour C, Dumesnil K and Mangin Ph 2000 *Phys. Rev.* B **62** 9517
[13] Mougin A 1999 *PhD Thesis* Institut National Polytechnique de Lorraine, France
[14] Huth M and Flynn C P 1998 *J. Appl. Phys.* **83** 7261
[15] Huth M and Flynn C P 1998 *Phys. Rev.* B **58** 11526
[16] Sawicki M, Bowden G J, de Groot P A J, Rainford B D, Beaujour J-M L, Ward R C C and Wells M R 2000 *Phys. Rev.* B **62** 5817–20
[17] Ciria M, Arnaudas J I, Dufour C, Oderno V, Dumesnil K and del Moral A 1997 *J. Appl. Phys.* **81** 5699
[18] Arnaudas J I, de la Fuente C, Ciria M, Benito L, Dufour C, Dumesnil K and del Moral A 2002 *J. Magn. Magn. Mater.* **240** 389
[19] de la Fuente C, Arnaudas J I, Ciria M, del Moral A, Dufour C and Dumesnil K 2009 *Appl. Phys. Lett.* **94** 132503
[20] de la Fuente C, Arnaudas J I, Ciria M, del Moral A, Dufour C, Mougin A and Dumesnil K 2001 *Phys. Rev.* B **63** 054417
[21] Hutchings M T 1964 *Solid State Physics* vol 16, ed F Seitz and D Turnbull (New York: Academic) p 227
[22] de Lacheisserie Ed T 1993 *Magnetostriction: Theory and Applications of Magnetoelasticity* (Boca Raton, FL: CRC Press)
[23] del Moral A 2008 *Handbook of Magnetostriction and Magnetostrictive Materials* (Algazara SL: Del Moral Publisher)
[24] Timoshenko S and Woinowsky-Kriger S 1959 *Theory of Plates and Shells* vol 2 (New York: McGraw-Hill)
[25] Nan C-W and Weng G J 1999 *Phys. Rev.* B **60** 6723
[26] Tefft W E 1966 *J. Res. NBS 70A-403, (Phys. and Chem.)* **4** 277
[27] Cullen J and Clark A 1977 *Phys. Rev.* B **15** 4510